Available online at www.sciencedirect.com
SCIENCE DIRECT®
International Journal of Thermal Sciences 42 (2003) 267–282
International Journal of Thermal Sciences
www.elsevier.com/locate/ijts

# Heat transfer in a radially rotating square duct fitted with in-line transverse ribs

S.W. Chang [a,*], W.D. Morris [b]

[a] *Department of Marine Engineering, National Kaohsiung Institute of Marine Technology, No. 142, Hai-Chuan Road, Nan-Tzu District, Postcode: 811, Kaohsiung, Taiwan, ROC*

[b] *Department of Mechanical Engineering, University of Wales, Swansea, Singleton Park, Swansea, SA2 8PP, UK*

Received 22 March 2002; accepted 3 May 2002

**Abstract**

This paper describes an experimental study of heat transfer in a radially rotating square duct with two opposite walls fitted by transverse ribs. The manner in which rotation modifies the forced heat convection is considered for the case where the duct rotates about an axis perpendicular to the duct's axis of symmetry and the flow within is radially outward with particular reference to the design of a gas turbine rotor blade. A selection of experimental results illustrates the individual and interactive effects of Coriolis and centripetal buoyancy forces on heat transfer along the centerline of each rotating rib-roughened surface. A number of experimental-based observations are revealed those confirm the manner for which the Coriolis force and centripetal buoyancy interactively modify the heat transfer even if the rib associating flow phenomena persist when the through flow transverses the ribs. An empirical correlation based on theoretical consideration and experimental data, which is physically consistent, has been developed to permit the evaluation of interactive effects of rib-flows, convective inertial force, Coriolis force and centripetal buoyancy on heat transfer.


*Keywords:* Rotating; Ribbed; Duct; Flow; Turbine; Rotor; Blade; Cooling

## 1. Introduction

The gas turbine engine has become an attractive prime mover for aeronautical crafts due to its high power-to-weight ratio, quick starting capability and reliable operation. The current gas turbine engine takes the advantage of thermodynamic benefit by operating the turbine entry temperature at the extremely high level, which is well above the melting point of material used. The air-cooling networks are thus essential to be incorporated inside the hot components of engine, especially within the highly stressed turbine rotor blade. These internal cooling networks within which the cooling air bled from the compressor is channeled are extremely complex. Fig. 1 typifies the arrangement of coolant passages in a modern high-pressure turbine rotor blade. As shown, the coolant channels roughened by the repeated ribs are connected in the multi-pass feature so that the coolant can flow radially outward or inward as it progresses through the blade. The film and transpiration cooling methods, with cooling air bleeding from the internal coolant passages via the tiny holes drilled through the blade, are utilized to facilitate the external blade cooling in a number of locations where the locally high heat fluxes are transferred from the gas stream. Because a turbine rotor blade rotates, the theoretical and experimental-based methods developed for predicting the forced convection in a stationary duct are known to be inaccurate for the design of the internal cooling passages of a turbine rotor blade.

When the coolant flows through theses cooling passages, it is constrained to rotate with the channel, giving rise to Coriolis and centripetal forces, which interactively change the nature of non-rotating flow field and therefore the internal heat transfer performance. The Coriolis forces, derived as the vector cross product of the angular velocity of the rotating duct and the flow velocity relative to the rotating duct, mainly create the secondary flows in the planes perpendicular to the channel axis and act as a source term in the momentum conservation equation to generate vorticity. In many instances, the Coriolis-induced secondary flow generates peripheral heat transfer variations

* Corresponding author.
*E-mail address:* swchang@mail.nkimt.edu.tw (S.W. Chang).

1290-0729/02/$ – see front matter 
doi:10.1016/S1290-0729(02)00026-1

**Nomenclature**

*English symbols*

| | |
|---|---|
| $A$ | coefficient |
| $a_i$ | smooth entry length of ribbed test duct ..... m |
| $a_e$ | plain exit length of ribbed test duct ..... m |
| $Bu$ | Buoyancy number |
| $C_i$ | coefficients |
| $C_p$ | specific heat of fluid ..... $J{\cdot}kg^{-1}{\cdot}K^{-1}$ |
| $D_h$ | hydraulic diameter of test duct ..... m |
| $e$ | rib height ..... m |
| $H$ | eccentricity ..... m |
| $k$ | thermal conductivity of fluid ..... $W{\cdot}m^{-1}{\cdot}K^{-1}$ |
| $L$ | active heating length of test duct ..... m |
| $l$ | rib land ..... m |
| $N$ | rotating speed of duct ..... $rev{\cdot}min^{-1}$ |
| $Nu$ | rotational Nusselt number |
| $Nu_0$ | stationary Nusselt number |
| $Nu_\infty$ | Nusselt number value for stationary developed turbulent duct flow |
| $n$ | exponent |
| $\vec{n}$ | unit direction vector of position vector, $\vec{r}$ |
| $P$ | rib pitch |
| $P$ | dimensionless pressure of flow in rotating duct |
| $p$ | pressure of flow in stationary duct ..... $N{\cdot}m^{-2}$ |
| $p^*$ | pressure of flow in rotating duct ..... $N{\cdot}m^{-2}$ |
| $Pr$ | Prandtl number |
| $q$ | convective heat flux ..... $W{\cdot}m^{-2}$ |
| $Re$ | Reynolds number |
| $Ro$ | Rossby number |
| $\vec{r}$ | position vector ..... m |
| $S$ | height of square ribbed duct ..... m |
| $T_0$ | fluid reference temperature ..... K |
| $T_f$ | fluid bulk temperature ..... K |
| $T_w$ | wall temperature of test duct ..... K |
| $V$ | dimensionless flow velocity |
| $v$ | flow velocity ..... $m{\cdot}s^{-1}$ |
| $W$ | width of square ribbed duct ..... m |
| $W_m$ | mean through flow velocity ..... $m{\cdot}s^{-1}$ |
| $xyz$ | coordinates of rotating reference frame |
| $z$ | axial location ..... m |
| $Z$ | dimensionless axial location |

*Greek symbols*

| | |
|---|---|
| $\beta$ | thermal expansion coefficient of fluid .... $K^{-1}$ |
| $\omega$ | angular velocity of rotating duct ..... $s^{-1}$ |
| $\Omega$ | dimensionless angular velocity of rotating duct |
| $\rho$ | fluid density ..... $kg{\cdot}m^{-3}$ |
| $\rho_0$ | fluid density at reference temperature . $kg{\cdot}m^{-3}$ |
| $\mu$ | fluid dynamic viscosity ..... $kg{\cdot}s^{-1}{\cdot}m^{-1}$ |
| $\varepsilon$ | dimensionless eccentricity |
| $\eta$ | dimensionless fluid temperature |
| $\Psi, \varphi_1, \phi_1, \phi_2$ | unknown functions |

*Subscripts*

| | |
|---|---|
| L | refers to centerline of rotating leading surface |
| T | refers to centerline of rotating trailing surface |
| 0 | refers to non-rotating situation |

around the duct and provides, respectively, the heat transfer enhancement and impediment relative to the non-rotating heat transfer level on its destabilized and stabilized surfaces. The centripetal force is itself hydrostatic to modify the pressure field from the static isothermal duct flow situation. When heat transfer takes place in the rotating flow field, the interaction of centripetal force with the disturbed coolant density caused by the coolant's temperature variations gives rise to a "free convection" like buoyancy effect which further modifies the flow structure and therefore the heat transfer. These two physical manifestations of rotation create vorticity and modify the turbulent structure of flow making the theoretical prediction of flow and heat transfer extremely difficult, despite the fact that the heat transfer enhancement for an internally cooled gas turbine rotor blade has being consistently pursued over the thirty years. Due to the engineering significance of flow in the rotating channels, the research works involve both theoretical and experimental studies of simplified models of the real cooling system in a turbine rotor blade [1–18]. The geometry of rotating channel relevant to the cooling conditions of a gas turbine rotor blade, such as the cross-sectioned shape [3,6,9,16], the patterns of surface ribs [8,10,13,18], the channel orientation [9,10,15] and the wall heating conditions [12,15], at various parametric test ranges have been examined to study their effects on heat transfer. The dimensionless parameters those control the heat transfer mechanism in a rotating channel have been agreed as the Reynolds number, $Re$, inverse Rossby number, $1/Ro$, and the rotating buoyancy parameter which, respectively, quantify the relative strengths of forced convective inertia, Coriolis force and the centripetal buoyancy. However, it still remains as a difficult goal to generate the laboratory scale simulations with Reynolds number, inverse Rossby number and rotating buoyancy parameter matching the realistic engine conditions simultaneously. The experimental data generated in the rotating channels with $Re \geqslant 10\,000$ and $1/Ro \geqslant 0.5$ were only those conducted at high test-pressures [4,9,10,13,16, 17]; and only in the last decade that the combined effect of surface ribs and rotation on heat transfer [8,10,13–15,18] were examined.

The strategic aim of this study is to develop an engineering methodology that could lead to the generation of the physically consistent heat transfer correlation, which is applicable for the design of the rib-roughened cooling passage in a gas turbine rotor blade. The formulation of the physical

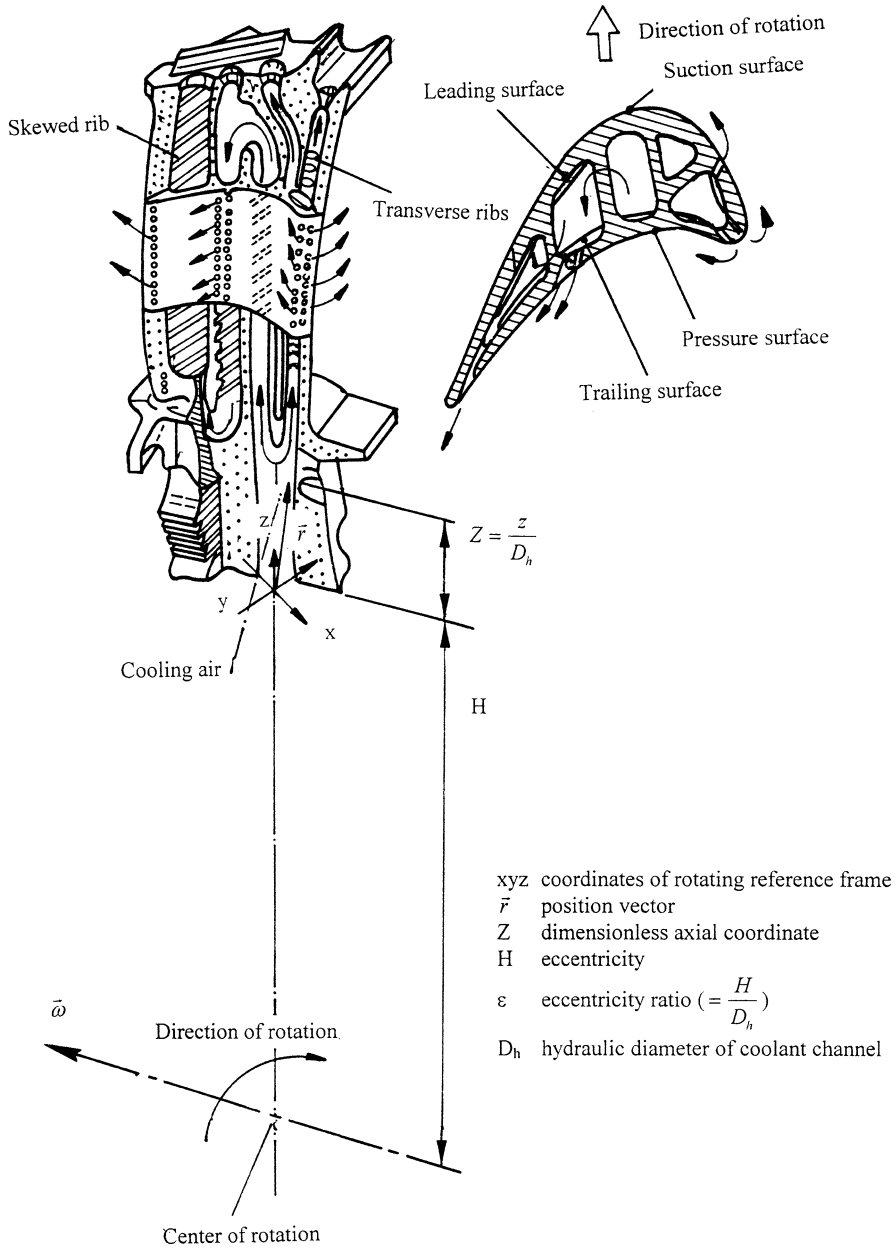


Fig. 1. Modern gas turbine rotor blade cooling channel network and coordinate system defined.

problem initiates from a study of the flow momentum equation in a rotating channel. The fluid motion is referred to a coordinate frame that itself rotates with the rotor blade so that the additional rotation-induced forces and their consequential effects on the momentum balance of fluid motion are considered. The dimensionless version of the modified Navier–Stoke equation, suitable for describing the fluid motion referred to a generalized rotating frame of reference, identifies a number of non-dimensional groups that control the convective flow in a rotating channel. The typical engine conditions are parametrically described in terms of these non-dimensional groups. These parametric engine conditions establish the references for the rig simulation, the parametric matrix tested and the data processing method developed. The range of the present experimental parameters reaches the representative gas turbine engine conditions. The local heat transfer data along the centerlines of two opposite rib-roughened rotating surfaces has been generated and correlated. The heat transfer physics in association with the individual and interactive effects of convective inertial force, Coriolis force and the centripetal buoyancy force are illustrated during which the empirical heat transfer correlation is developing. A set of empirical heat transfer correlations derived from the experimental data, which could uncouple the individual but mutually interactive effects of Coriolis and centripetal buoyancy forces, provides the physical and numerical consistencies between the correlative results and the actual heat transfer measurements.

## 2. Experimental strategy

### 2.1. Theoretical considerations

Fig. 1 also depicts the rotating coordinate system ($xyz$), the leading and trailing surfaces of a turbine rotor blade, the eccentricity ($H$), and the angular velocity ($\omega$) of the turbine rotor blade specified for the present study. Note that the frame of reference, $xyz$, rotates synchronically with the turbine rotor blade. The motion of fluid in any of the rotating coolant channels shown in Fig. 1 is controlled by the momentum conservation equations. The inertial acceleration of coolant has to be modified to account for the Coriolis and centripetal accelerations when the rotating reference frame, $xyz$, is employed to describe the fluid motion. The vector form of the flow momentum equation referred to the rotating coordinate system has been derived as [2]:

$$\frac{Dv}{Dt} = -\frac{1}{\rho}\nabla p + \mu\nabla^2 v - 2\omega \times v - \omega \times \omega \times \vec{r} \tag{1}$$

All symbols are defined in the Nomenclature. The last two terms of Eq. (1) represent the Coriolis and centripetal accelerations, respectively. The dynamic and hydrostatic natures, respectively, for the Coriolis and centripetal force-components are demonstrated by their own vector identities. The Coriolis force can only arise when the cross product of $\omega \times v$ exits. The flow velocity component in parallel with the direction of rotating vector, $\omega$, has no contribution to the generation of Coriolis force. As the direction of Coriolis force depends on the direction of local flow velocity, $v$, the Coriolis forces are, respectively, directed toward the trailing and leading surfaces of a rotating channel when the coolant flow is radially outward and inward. The so-called Coriolis secondary flows develop on the plane perpendicular to the main flow stream, which cause the fluid to spiral in the cooling passage [2] and drive the relative cooler fluid form the central core of flow toward the de-stabilized surface of the rotating channel. After reaching the destabilized surface, the coolant then circulates toward the opposite stabilized surface along the periphery of a rotating channel. When the coolant washes the heated wall, the fluid temperature gradually increases that gives rise the peripheral heat transfer variation in a rotating channel. The centripetal acceleration, $\omega \times \omega \times \vec{r}$, is irrelevant to the flow velocity but always directed toward the center of rotation. The magnitude of the centripetal acceleration increases when the fluid travels away from the center of rotation. Therefore the centripetal acceleration forms a conservative field and only contributes to the "hydrostatic" effect in the pressure field when the flow is isothermal. With the rotating heated flow over which the temperature-dependent density variation of fluids prevails, the centripetal acceleration could generate the additional effects via the buoyant interactions with the mechanism similar to the free convection motivated by the earth gravity [19]. But the centrifuge experienced in the rotating channel could be the order of $10^5$ earth gravity which causes the considerable effect on the forced convection. To identify the centripetal buoyancy interaction and its consequential effects on the fluid motion, the Boussinesq approximation is initially treated to express the local fluid density, $\rho$, as a temperature dependent function of

$$\rho = \rho_0\big(1 + \beta(T - T_0)\big) \tag{2}$$

where $\rho_0$ is the fluid density at a reference temperature $T_0$. Substitute Eq. (2) into Eq. (1) and retain the buoyant interaction with the centripetal acceleration term only yield the flow momentum equation to:

$$\frac{Dv}{Dt} = -\frac{1}{\rho}\nabla p^* + \mu\nabla^2 v - 2\omega \times v - \beta(T - T_0)\big(\omega \times \omega \times \vec{r}\big) \tag{3}$$

In Eq. (3), the so-called centripetal buoyancy term, $\beta(T - T_0)(\omega \times \omega \times \vec{r})$, couples with the fluid temperature field, $T(x, y, z)$; which solution is controlled by the energy equation of flow and varies with the thermal boundary condition. Because the temperature of coolant varies over the flow field, the effect of centripetal acceleration no longer remains hydrostatic in a rotating heated channel. Substitution of the non-dimensional parameters defined in Eqs. (4)–(8) into the momentum and energy equations of flow with the coordinates referred to the rotating frame of reference, $xyz$, obtains the dimensionless Eqs. (9) and (10) which, respectively, express the conservation laws of momentum and energy for the rotating flow.

$$V = \frac{v}{W_m} \tag{4}$$

$$\Omega = \frac{\omega}{N} \tag{5}$$

$$\eta = \frac{T - T_0}{T_w - T_0} \tag{6}$$

$$P = \frac{p^*}{\rho W_m^2} \tag{7}$$

$$\varepsilon = \frac{H}{D_h} \tag{8}$$

$$\frac{DV}{Dt} = -\nabla P^* + \frac{1}{Re}\nabla^2 V - \frac{1}{Ro}(2\Omega \times V) - Bu(\Omega \times \Omega \times \vec{n}) \tag{9}$$

$$\frac{D\eta}{Dt} = \frac{1}{Re\,Pr}\nabla^2 \eta \tag{10}$$

where $\vec{n}$ is the directional unit vector of the position vector, $\vec{r}$, and

$$Re = \frac{\rho W_m D_h}{\mu} \quad \text{Reynolds number} \tag{11}$$

$$Ro = \frac{W_m}{N D_h} \quad \text{Rossby number} \tag{12}$$

$$Bu = \frac{\beta(T_w - T_0)(Z+\varepsilon)}{Ro^2} \quad \text{Buoyancy number} \quad (13)$$

$$Pr = \frac{\mu C_p}{k} \quad \text{Prandtl number} \quad (14)$$

As an attempt to quantify the local buoyancy level in a rotating channel, the reference fluid temperature shown in Eq. (13), $T_0$, is selected as the local flow bulk temperature, $T_f$. To close Eqs. (9) and (10) for solving the flow and temperature distributions in a rotating channel requires a set of specified geometrical, flow and thermal boundary conditions. These boundary conditions are pre-defined once the experimental apparatus is built. The variation of any governing parameters, such as *Re*, *Ro*, *Bu* and *Pr* in Eqs. (9) and (10), results in the different solutions of flow and temperature fields. Accordingly the heat convective capability in a rotating channel varies. Such heat transfer variation corresponding to the systematic change of each of the governing flow parameters summarized from Eqs. (11) to (14) could reveals the heat transfer physics in associating with each varying parameter. Because the limiting case of zero rotating speed causes the Rossby number approaches infinite, the relative strength of Coriolis force to the convective inertial force is alternatively specified as the inverse Rossby number, $1/Ro$. Within the temperature range tested by the present study, the maximum variation in Prandtl number of tested coolant (dry air) is negligible about 0.66%. Therefore the strategic approach of this study is to disclose the functional relationship of

$$Nu = \Psi\{Re, 1/Ro, Bu, Z\} \quad (15)$$

where the experimentally defined Nusselt number, *Nu*, is calculated as

$$Nu = \frac{q D_h}{k(T_w - T_f)} \quad (16)$$

The convective heat flux, $q$, in Eq. (16) is obtained by subtracting the external heat loss from the total heat flux generated. A set of pre-calibration runs aimed at revealing the functional relationships of external heat loss with the wall-to-ambient temperature difference and the rotating speed is performed. Having defined the convective heat flux, $q$, the one-dimensional finite difference representation of Fourier conduction law is applied to correct the wall-temperature measurement to the inner plain-wall surface. The local enthalpy balance is also accounted at each measurement location to determine the flow bulk temperature, $T_f$. All the fluid properties used to define the dimensionless parameters in Eq. (15) are consequently evaluated at the local flow bulk temperature level.

Each of the independent variables in Eq. (15) is used as a measure to typify the engine representative conditions in the respect of gas turbine rotor blade cooling application. A detailed description of the experimental program formulated to study the effects of rotation on heat transfer in a radially rotating square duct fitted with rib-roughened leading and trailing walls now follows.

### 2.2. Rig simulation and experimental details

The high rotating speed of a gas turbine engine in the range of 5 000–20 000 rev·min$^{-1}$ proposes the extreme difficulty to attempt a full coverage of the engine representative conditions for any rig simulation. As an attempt to bring the experimental conditions to a part of nominal engine conditions, the design philosophy of experimental test rig is to reduce the mean flow velocity, $W_m$, with the coolant mass flow rate unchanged by increasing the pressure of flow inside the rotating channel. This approach increases the values of inverse Rossby number and consequently the buoyancy number by reducing the mean through flow velocity at any specified Reynolds number. The experimental conditions with relatively high inverse Rossby and buoyancy numbers thus become attainable when the rotating speed of test rig controls in the range of 1 000–2 000 rev·min$^{-1}$. The results of consultation with the aeronautical industries concerning the geometry, the flow range, rotating speed and temperature parameters, which provides the raw data for defining the typical range of dimensional and non-dimensional engine conditions in a coolant channel of gas turbine rotor blade, are summarized in Table 1 [20]. Also compared in Table 1 are the rig simulation conditions, which have been considerably extended from the past research works [5–8,11,12,14] due to the high-pressure level tested.

In the ranges of non-dimensional parameters simulated by the present test rig shown in Table 1, two different sets of data were generated from the rotating experiments. The first set of rotating data was produced at fixed Reynolds number in the range of 7 000–25 000. At each fixed Reynolds number, four rotational speeds, namely 0, 1 000, 1 500, and 2 000 rev·min$^{-1}$ were performed and the use of nozzles permitted the required Rossby number envelope to be covered. The results produced in this phase revealed the influence of inverse Rossby number (Coriolis force effect) on heat transfer. The other set of experiments controlled the inverse Rossby number constant in the range of 0–0.41 by adjusting the rotational speed. At each fixed Rossby number, heat transfer results with five Reynolds numbers of 7 000, 10 000, 15 000, 20 000 and 25 000 were obtained to show

Table 1
Typical engine and rig simulation conditions

| | Engine representative conditions | Rig simulation conditions |
|---|---|---|
| Engine speed (rev·min$^{-1}$) | 5 000–20 000 | 0–2 000 |
| Channel length (mm) | 40–250 | 110 |
| Channel hydraulic diameter (mm) | 3–7 | 9 |
| Mid-span eccentricity (mm) | 250–350 | 350 |
| Coolant entry temperature (K) | 700–1 000 | 303–313 |
| Coolant entry pressure (bar) | 10–15 | 3.5 max |
| Channel wall temperature (K) | 1 100–1 200 | 323–393 |
| Wall-to-fluid temperature ratio | 1.1–1.7 | 1.06–1.25 |
| Reynolds number (*Re*) | 100 000 max | 25 000 max |
| Inverse Rossby number ($1/Ro$) | 0–2 | 0–0.41 |
| Buoyancy number (*Bu*) | 0–40 | 0–1.2 |

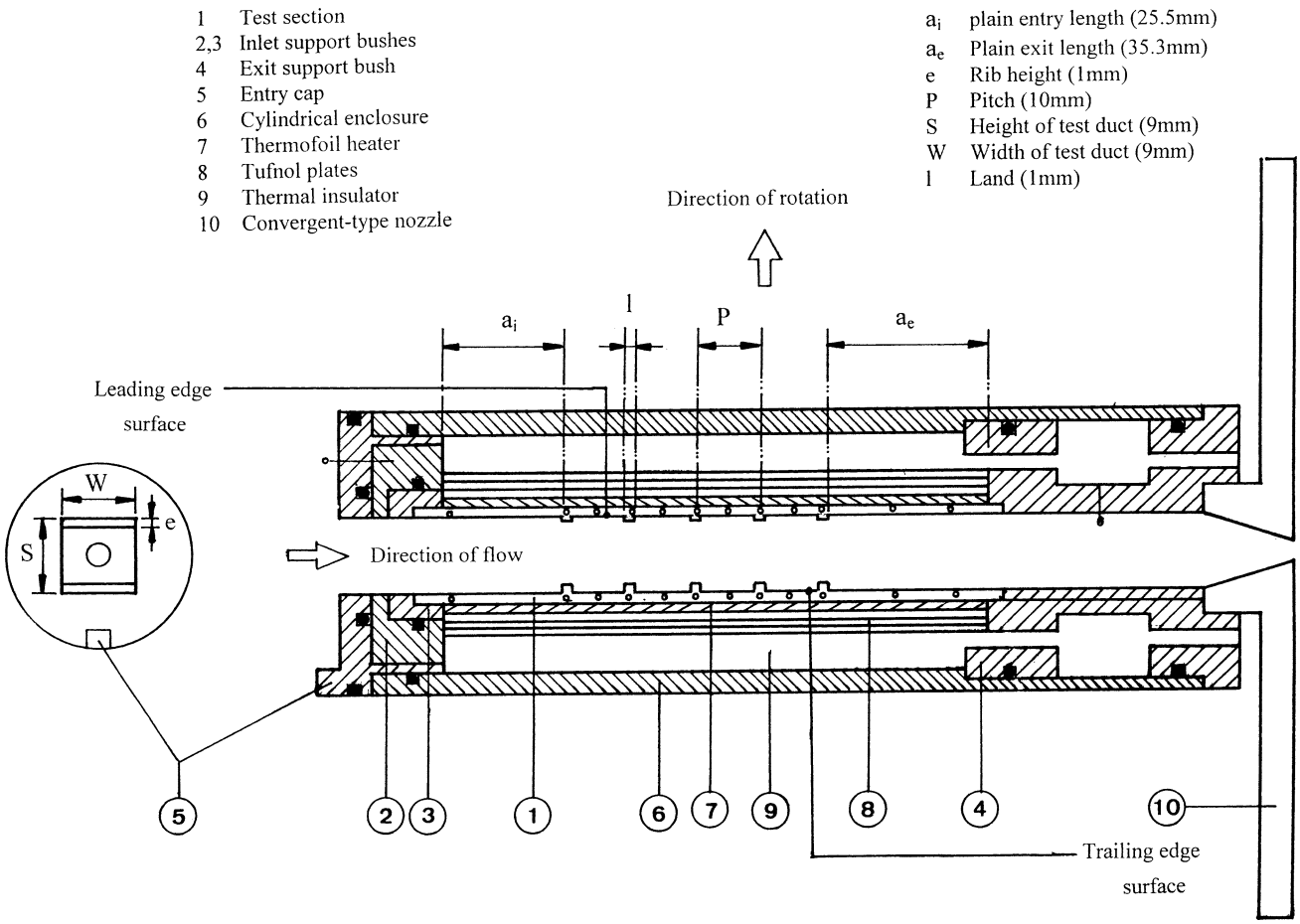


Fig. 2. Constructional details of heat transfer test module.

the Reynolds number effect (convective inertial force effect). To investigate the centripetal buoyancy effect, five ascending heater power levels to raise the wall temperature at the midspan location to 50°, 60°, 80°, 100° and 120 °C were used for each selected *Re*/*Ro* option. For each individual test, the flow and heater power were kept for about 30 min in order to assure the flow reached the steady state. The temporal wall temperature variations for several subsequent scans were less than ±0.3 °C when the flow was considered as steady state.

The overall experimental apparatus comprises a rotating facility onto which an assorted test section as shown in Fig. 2, which simulates a ribbed cooling passage in the gas turbine rotor blade, is attached. To create the rotating environment, the rotor system is driven by a DC electrical motor and housed in a soundproof test cell. The rotating facility in the speed range of 0–2 700 rev·min$^{-1}$ permits the pressurized air and the electrical heating powers to be fed into the test section. The thermocouple signals transmitted from the test section are connected with the Schlumberger SI3535D type data acquisition system via an integral instrumentation slip ring assembly. An on-line condition-monitoring program scans the rig simulating conditions in terms of the non-dimensional groups of *Re*, $1/Ro$ and *Bu* by processing the measured raw data. A full description of this rotating apparatus has been previously reported in [17]. A detailed description of the heat transfer test section now follows.

Fig. 2 shows the square ribbed test duct. Five sets of in-line square transverse ribs are fitted along each of the leading and trailing surfaces with regular downstream interval. The heated square duct (1), made of 2-mm-thick stainless steel plates, is held between the insulated bushes (2), (3) and (4). The inner width of this square duct is 9 mm. The rib pitch is 10 mm and each of these five transverse ribs, machined onto the inner face of duct wall, has a land of 1 mm. A smooth heated wall nominally 25.5 mm long proceeds the first rib. Another smooth-walled heating length of 35.5 mm is incorporated downstream of the final rib. The geometrical specifications of this test duct are described in terms of six non-dimensional groups defined in Fig. 2 as

Smooth entry length/hydraulic diameter ratio

$(a_i/D_h) = 2.83$

Plain exit length/hydraulic diameter ratio

$(a_e/D_h) = 3.94$

Rib height/hydraulic diameter ratio

$(e/D_h) = 0.11$

Rib pitch/rib height ratio

$(P/e) = 10.0$

Land/rib pitch ratio

$(l/P) = 0.1$

Aspect ratio

$(S/W) = 1.0$

The coolant passages centered in the inlet bushes (2), (3), and the entry cap (5) are carefully milled into the square section in order to avoid the upstream flow effects due to the change of duct geometry. The complete test assembly is enclosed in an aluminum tube (6) fitted with silicon "O" ring seals. The eccentricity measured at the cross-sectional plane where the heating commences is 295 mm. An electrical Minco thermal-foil heater (7), having a total heating length of 110 mm, is squeezed on each of the outer surface of the square duct. To secure these four heating foils on the outer surfaces of test duct (1), several layers of tufnol plates (8) are tightened on the top of each heating foil by threads. The silicone RTV form-type thermal insulation material (9) is filled between the encapsulating sheath and the test section to minimize the external heat loss. A convergent-type nozzle (10) is fitted at the flow exit so that the high-pressure tests could be performed.

Fitting the 9 mm wide test duct into a hollow 40 mm diameter plenum chamber of the rotating rig simulates a sharp flow entrance. The abrupt entry area ratio from the air plenum to the square test duct is about 15 : 1. The hydraulic boundary layers are re-developed from the sharp flow entrance. As shown in Fig. 2, the commencement of heating elements is fairly close to the sharp flow entrance that allows the simultaneous developments of thermal and hydraulic boundary layers in the developing flow regime with fairly uniform inlet velocity fields at the flow entrance.

Twelve type-K thermocouples are mounted along each of the two axial centerlines of the leading and trailing rib-roughened surfaces. These thermocouples are embedded in the duct wall with their sensing junctions 0.5 mm away from the plain inner surface of the test duct. The axial distribution of these thermocouples is set such that its location corresponds precisely to the center or mid-pitch locations of the ribs. As it is attempted to avoid the disturbance of flow inside the rotating duct, only two additional thermocouples are installed in the inlet and exit insulator bushes (2) and (4), respectively, to measure the flow entrance and exit temperatures for the subsequent assessment of fluid temperature rise due to heat transfer. The evaluated flow bulk temperature at the exit plane is checked with the actual measurement. The agreement between the evaluated and measured flow bulk temperatures at the exit plane could confirm the accuracy of instrumentation. Any batch of the experimental raw data could be accepted for the subsequent data processing provided that the difference between the evaluated and measured flow bulk temperatures at the exit plane is less than $\pm 10\%$.

The uncertainty analysis reveals that the most of experimental uncertainties in calculating Nusselt number are attributed from the temperature measurement. As the fluid properties such as the fluid viscosity and thermal conductivity are estimated using the temperature dependent evaluation equations, the uncertainty in temperature measurement also results in uncertainties of *Nu*, *Re*, *Ro* and *Bu*. The estimated maximum uncertainties for *Nu*, *Re*, *Ro* and *Bu* are about 11%, 5.2%, 4.8% and 5.2%, respectively [21]. Also indicated by the uncertainty analysis is the improved accuracy for the higher level of heat flux tested.

## 3. Results and discussion

### 3.1. General observations

To reveal the functional relationship of Eq. (15) is the strategic aim of the present study. The heat transfer results obtained in the static duct are initially analyzed and compared with the relevant previous results for commissioning the present experimental methods and subsequently correlated to provide the references against which the rotational effects on heat transfer are assessed. Fig. 3 depicts the axial distributions of normalized Nusselt number, $Nu_0/Nu_\infty$, along the rib-roughened surfaces of static duct. Also compared in Fig. 3 are the heat transfer results of Han et al. [22] and Johnson et al. [10], which test geometries share great similarities with the present study. Note that, to be comparable with the data of Han et al. [22] and Johnson et al. [10], the Dittus-Boelter heat transfer level, $Nu_\infty$, calculated as $0.023Re^{0.8}Pr^{0.3}$ [22], is selected to normalize the Nusselt number in the static duct, $Nu_0$. As shown in Fig. 3, the present data shows good agreements with Johnson et al. [10]. Relative to the data of Han et al. [22], the agreements only appear in the further downstream locations ($Z > 8$). The discrepancy between the present results and the data of Han et al. [22] in the flow entry region mainly attributes from the different location of the first rib. In this respect, a detailed illustration describing the effect of the first rib location on the heat transfer in the developing flow region of the static rib-roughened square duct is provided in [24]. As depicted in Fig. 3, the axial heat transfer variations over the rib-roughened surface exhibit the zig–zag pattern where the relatively high heat transfer level develops at the mid–rib location. The heat transfer enhancement to the level about 2.5 times of the Dittus–Boelter value [23] is generally achieved by fitting the in-line transverse ribs.

There is a systematic reducing tendency in $Nu_0/Nu_\infty$ when Reynolds number increases as shown in Fig. 3. The higher values of $Nu_0/Nu_\infty$ consistently occur at the lower Reynolds numbers. This particular result indicates that the correlation of $Nu_0$ no longer follows the $Re^{0.8}$ relationship but the exponent of Re is less than 0.8 in the rib-roughened duct. In the static duct, the force ratios quantified by the inverse Rossby and buoyancy numbers in Eq. (15) are not

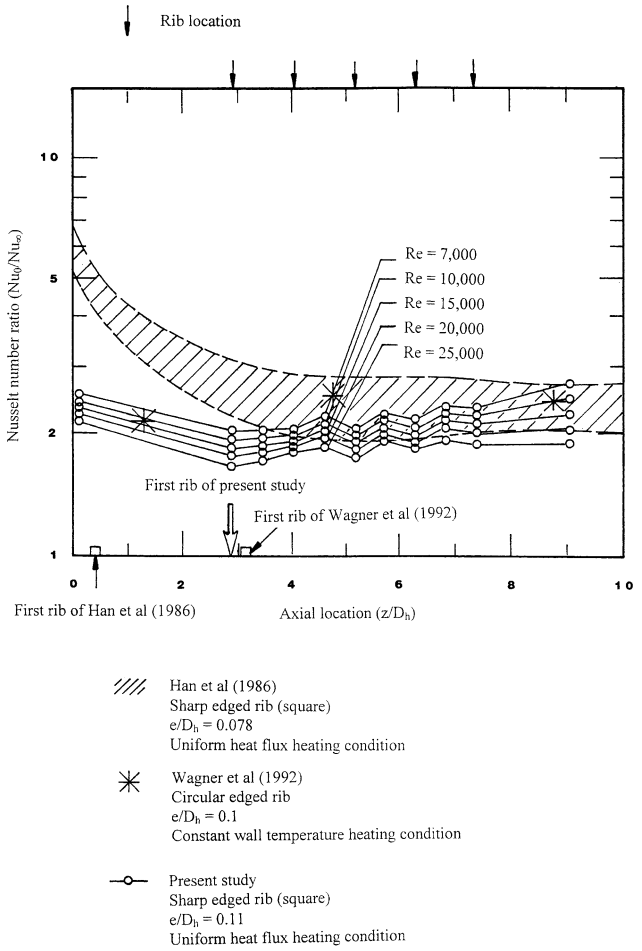


Fig. 3. Comparison of stationary heat transfer results with Han et al. (1986) and Wagner et al. (1992).

involved in the heat transfer physics so that the local Nusselt number, $Nu_0$, could be correlated by Reynolds number alone when the Prandtl number of fluid remains constant. To comply with the limiting case of vanished forced convective capability when Reynolds number approaches zero, the local Nusselt numbers in the static duct, $Nu_0$, at each rib and mid-rib location are correlated by Eq. (17).

$$Nu_0 = A(Z) \times Re^{n(Z)} \tag{17}$$

Because the present rig simulation considers the effect of abrupt entrance on the heat transfer in the developing flow regime, the coefficients $A$ and $n$ vary with the axial location, $Z$, to reflect the influence of boundary layer development on heat transfer. The axial variations of coefficients $A$ and $n$ could be, respectively, treated as the indications of the rib effects and the convective inertial force effect on heat transfer. Table 2 summarizes the correlated coefficients $A$ and $n$ along the rib-roughened surface. Note that, as the changes of heater power setting (buoyancy level) in the static duct could not cause the noticeable heat transfer variations at any axial location measured, the buoyancy effect in the static rib-roughened duct is negligible. The heat transfer values along the leading surface centerline are similar to the values of the trailing surface counterparts. Thus the data selected to generate Eq. (17) includes all the results obtained with various heating powers along the centerlines of leading and trailing surfaces.

Table 2
Correlative coefficients $A$ and $n$ for stationary Nusselt number, $Nu_0$

| Axial location | $Z$ | $A(Z)$ | $n(Z)$ |
|---|---|---|---|
| Flow entrance | 0.0 | 0.0683 | 0.786 |
| Rib 1 | 2.88 | 0.0649 | 0.7419 |
| Rib 2 | 4.0 | 0.0714 | 0.7355 |
| Rib 3 | 5.11 | 0.0819 | 0.7238 |
| Rib 4 | 6.22 | 0.0952 | 0.7145 |
| Rib 5 | 7.33 | 0.1260 | 0.6900 |
| Mid-rib 1-2 | 3.44 | 0.0781 | 0.7473 |
| Mid-rib 2-3 | 4.55 | 0.0765 | 0.7303 |
| Mid-rib 3-4 | 5.66 | 0.0950 | 0.7103 |
| Mid-rib 4-5 | 6.77 | 0.1103 | 0.7022 |

Table 2 demonstrates that the exponent, $n$, of Reynolds number in Eq. (17) decreases from an initial value of 0.79 toward 0.69 as the rib number increases. The exponent, $n$, of 0.79 at the sharp flow entrance approaches the well established 0.8 value for the smooth-walled turbulent duct flow [23]. The gradual reduction of n value in the downstream direction when the flow traverses the ribs indicates the weakened forced convective inertial effects on heat transfer. Accompanying with the streamwise decay of exponent, $n$, along the rib-roughened surface is the streamwise increase of coefficient $A$, which could be treated as an indication of the heat transfer enhancement due to the rib associated phenomena when the rib-induced flows gradually develop.

Having established the stationary heat transfer references of Eq. (17) against which the rotational data could be compared, the results obtained from the rotating tests are now examined. To describe the heat transfer physics in the rotating duct, Fig. 4 typifies a set of axial distributions of rotational Nusselt number, $Nu$, generated with five ascending heating levels along the centerlines of rib-roughened leading and trailing surfaces when the Reynolds and inverse Rossby numbers are, respectively, 8 000 and 0.2. The considerable data spreads at each measured axial spot are observed in Fig. 4 due to the variations of heat flux (buoyancy level). At this *Re–Ro* option, the local Nusselt numbers increase with the increased heat flux (buoyancy level). The rotating buoyancy effect in isolation enhances the local heat transfer at this particular set of *Re–Ro* option. Although the rotating buoyancy effect on heat transfer within the present parametric ranges tested provides consistent heat transfer enhancement along the centerlines of leading and trailing surfaces, the ranges of data spread at each axial location vary with the Rossby number. The dependency of buoyancy effect on Rossby number is implied which will be further examined when the rotating heat transfer results are parametrically described.

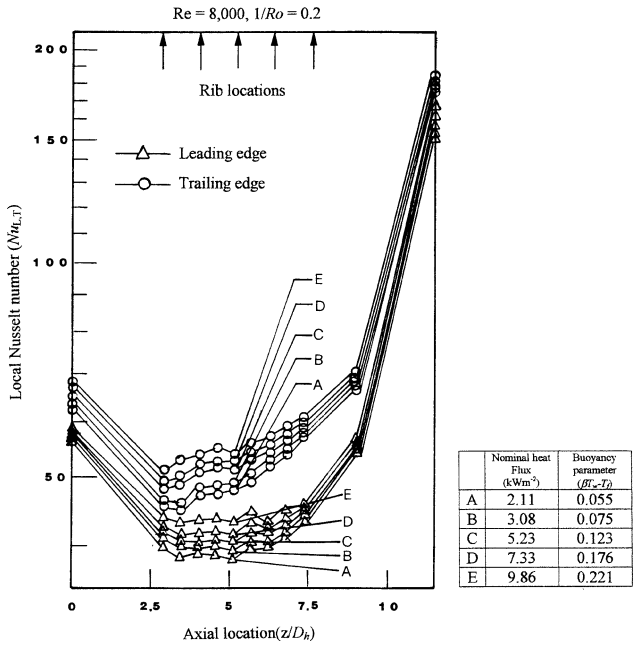


| | Nominal heat Flux ($kWm^{-2}$) | Buoyancy parameter ($\beta(T_w-T_f)$) |
|---|---|---|
| A | 2.11 | 0.055 |
| B | 3.08 | 0.075 |
| C | 5.23 | 0.123 |
| D | 7.33 | 0.176 |
| E | 9.86 | 0.221 |

Fig. 4. Typical axial distributions of rotating Nusselt number along centerlines of rib-roughened leading and trailing surfaces at Reynolds number of 8 000 and inverse Rossby number of 0.2.

Also clearly shown in Fig. 4 is the heat transfer differences between the leading and trailing surfaces so that the peripheral heat transfer variations are established when the duct rotates. The better heat transfer along the centerline of rotating trailing surface relative to its leading counterpart demonstrates a typical Coriolis-force effect. Note that the cyclical ripples in the axial heat transfer distributions induced by the transverse ribs found in the static duct are still present but the detailed saw-tooth patterns along the centerlines of leading and trailing surfaces vary when the duct rotates. The Coriolis forces couple with the considerable buoyancy interactions creating the peripheral flow fields, which interact differently with the rib-induced flows along the leading and trailing rotating surfaces. In Rothe and Johnston [1] that experimentally examined the radially rotating ribbed duct flow, a longer reattachment length was consistently found on the stable side (leading surface) relative to its unstable counterpart (trailing surface) due to the spatial variations of flow instability phenomena in a rotating rib-roughened channel. As the longer reattachment length normally reflects the relatively poor heat transfer, the heat transfer difference between the leading and trailing surfaces of a rotating ribbed duct is partially attributed from this mechanism. As usual with the forced convection experiments there is an end loss effect shown in Fig. 4, which causes the wall temperature to fall off over the final section of the test duct and results in the Nusselt number increments in the end region of the test duct. Therefore only the data generated in the region fitted with ribs ($Z \geqslant 7.33$) are further analyzed.

### 3.2. Parametrical presentation

The physics manifesting the forced convection from the rotating rib-roughened surface to fluids, namely the Coriolis force effect, the rotating buoyancy interaction and the inertial force effect, interact to produce the typical heat transfer results as depicted in Fig. 4. These dynamic force ratios, including the forced convective inertia, the Coriolis force and the centripetal buoyancy, are respectively quantified by Reynolds, inverse Rossby and buoyancy numbers which form the constituent components of Eq. (15). One of the strategic aims of the present study is to identify the functional relationships involved in Eq. (15). It is initially attempted to isolate the *Re* variable from Eq. (15). In Morris and Chang [17], the effect of Reynolds number on heat transfer in a radially rotating smooth-walled tube is isolated from the rotational parameters when Eq. (15) is normalized by $Re^{0.8}$. This approach is verified by comparing the different sets of normalized results in terms of $Nu/Re^{0.8}$ obtained with different Reynolds numbers at a selected *Ro*. Their results showed that the axial distributions of $Nu/Re^{0.8}$ obtained from different Reynolds numbers at a fixed Rossby number collapsed into the tight data bands when the buoyancy interactions remained at the approximately same level. Nevertheless, the rib-induced flow physics have modified the influences of *Re* on $Nu_0$ from the $Re^{0.8}$ relationship into $Re^{n(Z)}$ in the static duct where the exponent, $n$, varies with $Z$ to reflect the streamwise development of rib flows. The initial attempt made to isolate the *Re* effects from the rotational force effects by normalizing the rotational Nusselt number with $Re^{0.8}$ is not successful in this rib-roughened channel. The normalization of rotational Nusselt number with $Nu_\infty$ could not isolate the *Re* effects from the rotational force effects. Alternatively, the isolation of Reynolds number effects from *Ro* and *Bu* at any axial location is achieved by normalizing the rotational Nusselt number with $Re^{n(Z)}$. To demonstrate the isolation of *Re* variable from Eq. (15), two sets of illustrative examples are collected in Fig. 5, where the axial distributions of scaled Nusselt number in terms of $Nu/Re^{n(Z)}$ are produced from two different Reynolds numbers but at the same value of Rossby number. Note that the buoyancy level in terms of the buoyancy parameter, $\beta(T_w - T_f)$, for all the data collected in Fig. 5 is about 0.223. As shown in Fig. 5(a) and (b), the data generated with different Reynolds numbers at each inverse Rossby number of 0.09 or 0.14 collapses into the tight data band at each axial location. The convective force effect, quantified by the $Re^{n(Z)}$ relationship in Eq. (15), are demonstrated to be uncoupled from the rotational force effects when the *Nu* is normalized with the equation involving the $Re^{n(Z)}$ structure.

Also plotted in Fig. 5 are the axial variations of $Nu_0/Re^{n(Z)}$, which values correspond to the coefficients $A(Z)$ listed in Table 2. The comparison of the scaled Nusselt numbers between the data generated in the static and rotating ducts as shown in Fig. 5 indicates the interacting Coriolis

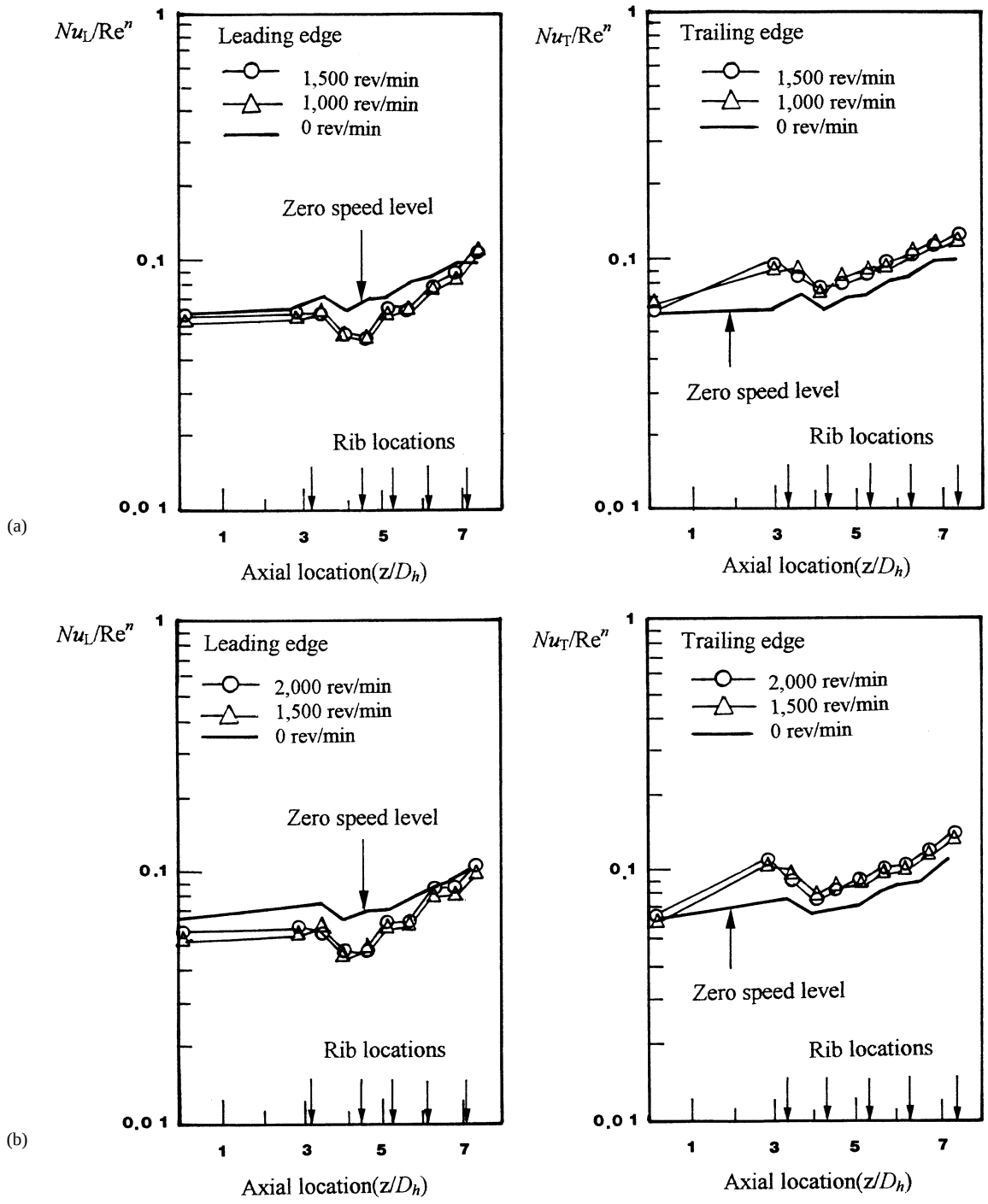


Fig. 5. Axial distributions of normalized Nusselt number, $Nu_{L,T}/Re^n$, at inverse Rossby numbers of 0.09 and 0.14. (a) $1/Ro = 0.09$; (b) $1/Ro = 0.14$.

and buoyancy force-effects on heat transfer since the Re effects have been isolated. Heat transfers along the centerlines of the rotating rib-roughened leading and trailing surfaces are, respectively, impeded and improved from the static duct levels. The increase of inverse Rossby number from 0.09 to 0.14, which enhances the relative strengths of rotational forces, provides the more profound heat transfer enhancement and impediment relative to the static heat transfer references along the centerlines of rotating trailing and leading surfaces respectively. The heat transfer enhancements along the rotating trailing surface centerline are evident in the smooth-walled entry region while the severe heat transfer impediments develop near the second rib and mid-rib locations on the leading surface. The dependency of rotational effects on the axial location is found and varied with the leading and trailing surfaces. In light of the collapsing

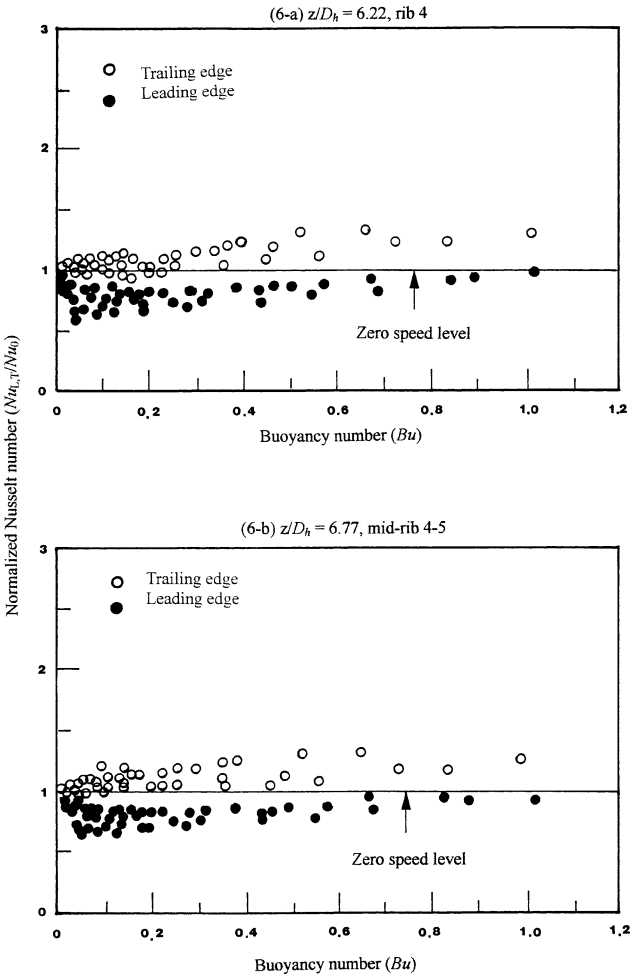


Fig. 6. Variations of normalized Nusselt number, $Nu_{L,T}/Nu_0$, with Buoyancy number at rib 4 and mid-rib 4-5.

tendency demonstrated in Fig. 5, the correlating equation of rotational Nusselt number along the centerlines of rib-roughened leading and trailing surfaces, $Nu_{L,T}$, is simplified as:

$$\frac{Nu_{L,T}}{Nu_0} = \varphi_1\left\{\frac{1}{Ro}, Bu, Z\right\} \tag{18}$$

where $\varphi_1$ is a to be determined function. However the complete axial heat transfer profiles along the rib-roughened surfaces are complicated which could not be fully identified using the limited thermocouples available. Thus Eq. (18) is only determined for the rib and mid-rib locations by the present study.

A parametric review of the combined Coriolis and buoyancy force-effects on heat transfer is typified in Fig. 6 where the scaled Nusselt numbers, $Nu_{L,T}/Nu_0$, are plotted against the buoyancy number, *Bu*, at the locations of rib 4 and mid-rib 4-5. The scaled Nusselt numbers, $Nu_T/Nu_0$, are all above the zero speed level ($Nu_T/Nu_0 = 1$) and constantly increase with *Bu* on the trailing surface. An initial heat transfer impediment on the leading surface that could lead the scaled Nusselt numbers, $Nu_T/Nu_0$, to the levels about 0.63 is found when *Bu* increases. Followed by the worst heat transfer scenarios on the leading surface shows a subsequent heat transfer recovery when *Bu* increases further. Over the entire range of parametric conditions tested, the most of Nusselt numbers detected from the leading surface are less than the referenced values in the static duct. These data trends are typical for those found at other axial locations, which also show consistency with the data, reported by other investigators [4,10,11,16,17].

Note that the data shown in Fig. 6 is collected from the entire parametric ranges tested. There are a number of Rossby numbers involved in Fig. 6. Therefore the scaled Nusselt numbers, $Nu/Nu_0$, at the limiting cases of $\beta(T_w - T_f) = 0$ and $Ro \neq 0$, which create the rotating zero buoyancy scenarios, shall not be unity but vary with *Ro* to reflect the individual Coriolis force effect on heat transfer. Although the data plot shown in Fig. 6 is useful to provide an overall review of the relative change in heat transfer compared to the stationary case, this parametric presentation of experimental data using *Bu* as a single variable suffers from the physical inconsistency. Fig. 7 attempts to generate the zero-buoyancy data by extrapolating five scaled Nusselt numbers, $Nu/Nu_0$, collected from a Rossby number toward the asymptotic value corresponding to zero buoyancy condition. As seen in Fig. 7 for each individual line that comprise five data points with ascending buoyancy levels at a fixed Rossby number, a linear-like increase of the scaled rotational Nusselt numbers is evident. The various slopes for these correlating lines shown in Fig. 7 indicate the different *Bu* effects on heat transfer when *Ro* varies. The existence of coupling effects between Coriolis force and centripetal buoyancy is demonstrated. The more pronounced buoyancy effect, characterized by the steeper increasing rate of the correlating line shown in Fig. 7, tends to be resolved with lower inverse Rossby numbers when the Coriolis force-effect is less dominant.

The zero buoyancy solution in a rotating channel is not strictly possible in practice since a heat transfer test requires a finite temperature difference between the duct wall and the fluid. Therefore the zero buoyancy Coriolis effects are inferred by extrapolating a family of heat transfer data taken at a specified Rossby number with five temperature differences between the wall and fluid to a zero temperature difference. This has been demonstrated in Fig. 7 as a representative case of $Z = 5.66$ (mid-rib 3-4). For all the axial locations considered and the entire range of inverse Rossby numbers tested, the zero buoyancy solution is obtained numerically using a linear curve fitting routine. This fit was found to be the most useful in preserving a sensible physical consistency. With examination of the heat transfer levels extrapolated to the zero-buoyancy situations shown in Fig. 8, these extrapolated limits continuously increase with the increase of inverse Rossby number on the trailing surface. At the leading surface shown in Fig. 8, the zero-buoyancy situation initially brings the heat transfer level from the stationary reference down to a cross over point

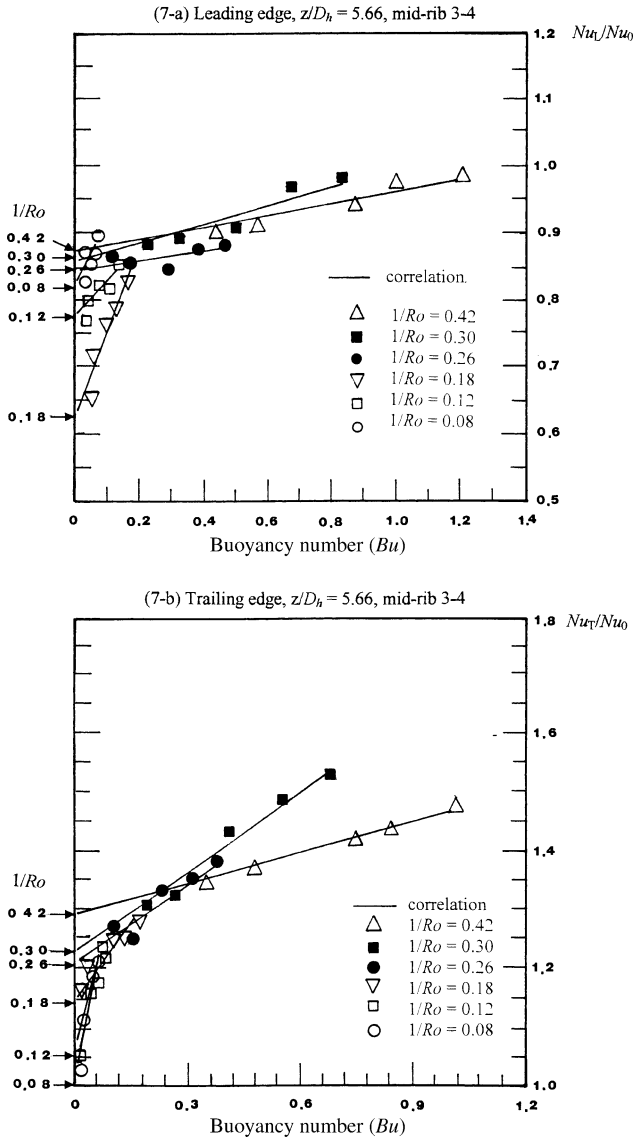


Fig. 7. Variations of normalized Nusselt number $Nu_{L,T}/Nu_0$, with Buoyancy number at various inverse Rossby number.

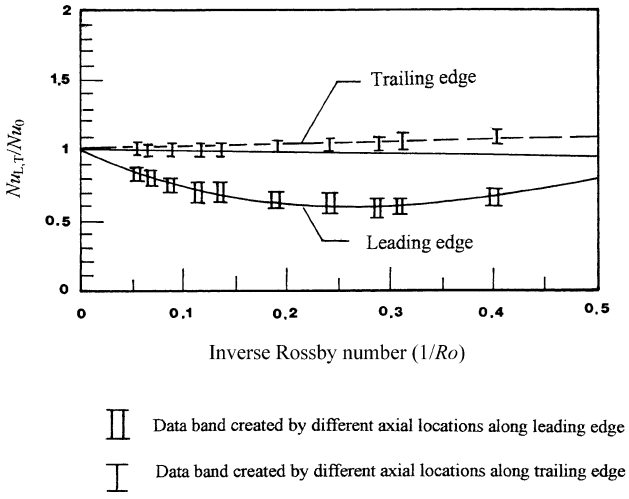


Fig. 8. Heat transfer variations with inverse Rossby number at zero buoyancy scenarios.

where a minimum heat transfer rate occurs. A subsequent heat transfer recovery then follows. This variation trend for the extrapolated zero-buoyancy limit match the experimental results of mass transfer in a rotating tube reported by Berg et al. [7]. Thus, acting by the Coriolis force alone without buoyancy interaction, the heat transfer on the leading surface is initially reduced after which a subsequent heat transfer recovery is followed. The buoyancy interactions on the leading and trailing surfaces consistently improve heat transfer from the zero-buoyancy base line created by the Coriolis forces within the parametric conditions examined.

The extrapolated zero buoyancy results over all ranges of axial locations are generated after applying the extrapolating procedure to the complete sets of experimental data which results could reveal the true Coriolis effects on heat transfer. Fig. 8 summarizes the variations of normalized Nusselt number, $Nu/Nu_0$, with inverse Rossby number for all the axial locations detected. It is interesting to note that, although the flow conditions for the rib and mid-rib locations are different, the zero-buoyancy solutions that characterize the Coriolis force-effects appear to be independent with the axial location. On the leading surface, the most of test results are covered with severe heat transfer impediment. Although the heat transfer is consistently improved on the trailing surface by the Coriolis force-effects, the considerable influences occur when the inverse Rossby number becomes greater than 0.2. On completion of the extrapolating procedure, these zero buoyancy heat transfer results are combined with the raw data for the subsequent data analysis leading to the generation of empirical heat transfer correlations.

### 3.3. Empirical heat transfer correlations

It has been revealed that the isolated effect of Reynolds number on heat transfer in the rotating rib-roughened duct is taken into account via $Re^{n(Z)}$ relationship. The influences of centripetal buoyancy on heat transfer vary with the relative strength of Coriolis forces as demonstrated in Fig. 7, which highlights the existence of coupling Coriolis and buoyancy force-effects on heat transfer. Acting by the Coriolis force alone, the heat transfer is consistently improved relative to the stationary level over the trailing surface. On the leading surface, the individual Coriolis force-effects reduce heat transfer from the static duct level at the lower values of inverse Rossby number but further increasing the inverse Rossby number follows a subsequent heat transfer recovery. To preserve the physical consistency of the empirical heat transfer correlations, the mathematical structure of Eq. (18) has to satisfy the following conditions. The function has to be unity when $1/Ro = 0$ that is the zero rotation limit at all axial locations. Also the coupling effects already noted between the inverse Rossby number and buoyancy number shown in Fig. 7 must be such that as the buoyancy number becomes zero the local Nusselt numbers must still be

functionally linked to the inverse Rossby number. The zero buoyancy case shall be true for example with the analogous case of mass transfer from the wall to the fluid. In this case, the Coriolis driven secondary flows and its related flow phenomena will still alter the mass transfer even in the absence of buoyancy. Examination of these physical restrictions on the mathematical structure of Eq. (18) and the linear-like data trends revealed in Fig. 7 led to the assumed structure given in Eq. (19) could be a possible format of correlative equation for heat transfer.

$$\frac{Nu_{L,T}}{Nu_0} = \phi_1\left\{\frac{1}{Ro}, Z\right\} + \phi_2\left\{\frac{1}{Ro}, Z\right\} \times Bu \tag{19}$$

$\phi_1$ and $\phi_2$ in Eq. (19) are functions of inverse Rossby number and the non-dimensional axial location and they respectively define the variations of Coriolis and buoyancy effect on heat transfer. Also the value of function $\phi_1$ has to be unity when $1/Ro$ equals zero. As illustrated in Fig. 7, the procedure of a standard regression using Eq. (19) is conducted in order to define the functions of $\phi_1$ and $\phi_2$ in Eq. (19). With all the measured data to be compared with the correlated results using Eq. (19) shows that the maximum discrepancy in this correlating stage is less than $\pm 5\%$. Evidence of this has been typified in Fig. 7 that the lines shown are linear regressions of the experimentally measured data in which the extrapolating zero-buoyancy levels are included. The assumed linear functional form of Eq. (19) with respect to the buoyancy number permits another simplification in the quest for the correlation of heat transfer.

Using a series cross plots based on Eq. (19) but applied to each measured rib and mid-rib locations, it is possible to interpolate a series of curves for the relative Nusselt number ratio against the inverse Rossby number for a range of buoyancy levels. For each rib and mid-rib locations over the range of axial locations measured, the manners in which functions $\phi_1$ and $\phi_2$ vary with the inverse Rossby number are revealed. The variations of $\phi_1$ and $\phi_2$ with inverse Rossby number at mid-rib 2-3 and rib 3 locations are depicted in Fig. 9 to illustrate their variation trends. Because the significance of buoyancy effect is alleviated when the Coriolis forces become more dominant that has been justified in Fig. 7 where the slope for each constant inverse-Rossby number line decreases with the increase of inverse-Rossby number, function $\phi_2$ thus continuously decreases with inverse Rossby number. Led by a detailed examination of all rib and mid-rib location versions of Fig. 9, it is proposed that $\phi_1$ and $\phi_2$ can be reasonably approximated by the equations of the following general form

$$\phi_1 = 1 + \frac{C_1(Z)}{Ro} + \frac{C_2(Z)}{Ro^2} \tag{20}$$

$$\phi_2 = C_3(Z) + C_4(Z)\exp\left(\frac{C_5(Z)}{Ro}\right) \tag{21}$$

In combination with Eq. (19), the constant 1 in Eq. (20) reflects the zero rotation effect when inverse Rossby number becomes zero. The function of $C_5$ in Eq. (21) is always negative that reflects the reducing buoyancy effect due to the increasing dominance of the Coriolis effect. These equation structures may be applied to the rib-roughened leading and trailing surfaces but with different $C$-functions. Tables 3 and 4 list the numerically determined curve fits for the $C$-functions along the centerlines of leading and trailing surfaces, respectively.

An empirical correlation based on a physical interpretation of the governing conservation equations of momentum and energy has been derived following an experimental approach to resolve the influences of rib and inertia force and the coupling effects of Coriolis and centripetal buoyancy forces on heat transfer. Comparing all the experimental measurements with the correlative predictions has performed as a review for the overall success of this empirical proposal. Over the entire range of parametric conditions studied, 93% of the present experimental Nusselt number data are found to agree within $\pm 18\%$ of the correlation proposed. Fig. 10 typifies the comparison of experimental and correlative results, where a selection of experimental data generated at inverse Rossby numbers of 0.07, 0.09, 0.1, 0.125, 0.3 and 0.32 from all the axial locations detected is compared with the empirical prediction. As shown, the correlative predictions appear to fit the data reasonably well, particular on the trailing edge. As usual, the extrapolation beyond the simulation conditions of the present study listed in Table 1 could give rise to uncertainties but the methodology developed for empirical prediction remains its applicability. Considering the complexities of the rotating rib-roughened duct flow, the proposed correlation should offer a good indication of the

Table 3
$C$-functions for leading surface centerline

| Rib/Mid-rib | $Z$ | $C_1$ | $C_2$ | $C_3$ | $C_4$ | $C_5$ |
|---|---|---|---|---|---|---|
| Rib 1 | 2.88 | −1.695 | 3.161 | 0.1824 | 5.342 | −14.52 |
| Rib 2 | 4.0 | −2.014 | 4.176 | 0.02941 | 2.908 | −9.166 |
| Rib 3 | 5.11 | −2.331 | 4.762 | 0.1375 | 3.057 | −11.73 |
| Rib 4 | 6.22 | −2.494 | 5.275 | 0.14 | 6.523 | −21.17 |
| Rib 5 | 7.33 | −2.411 | 5.091 | 0.1028 | 6.293 | −23.71 |
| Mid-rib 1-2 | 3.44 | −1.732 | 3.227 | 0.1011 | 2.466 | −8.309 |
| Mid-rib 2-3 | 4.55 | −2.056 | 4.003 | 0.1462 | 2.242 | −9.264 |
| Mid-rib 3-4 | 5.66 | −2.345 | 4.784 | 0.108 | 1.921 | −10.73 |
| Mid-rib 4-5 | 6.77 | −2.459 | 5.204 | 0.01943 | 1.432 | −7.942 |

Table 4
$C$-functions for trailing surface centerline

| Rib/Mid-rib | $Z$ | $C_1$ | $C_2$ | $C_3$ | $C_4$ | $C_5$ |
|---|---|---|---|---|---|---|
| Rib 1 | 2.88 | 0.0162 | 0 | 0.3912 | 4.922 | −18.86 |
| Rib 2 | 4.0 | 0.016 | 0 | 0.3581 | 3.222 | −11.51 |
| Rib 3 | 5.11 | 0.01613 | 0 | 0.3911 | 4.922 | −18.86 |
| Rib 4 | 6.22 | 0.0721 | 0 | 0.3193 | 12.24 | −35.98 |
| Rib 5 | 7.33 | 0.1096 | 0 | 0.1007 | 3.774 | −10.23 |
| Mid-rib 1-2 | 3.44 | 0.09363 | 0 | 0.2075 | 2.55 | −8.81 |
| Mid-rib 2-3 | 4.55 | 0.04579 | 0 | 0.1926 | 2.205 | −8.536 |
| Mid-rib 3-4 | 5.66 | 0.1617 | 0 | 0.2818 | 13.01 | −26.42 |
| Mid-rib 4-5 | 6.77 | 0.1786 | 0 | 0.2227 | 7.068 | −45.03 |

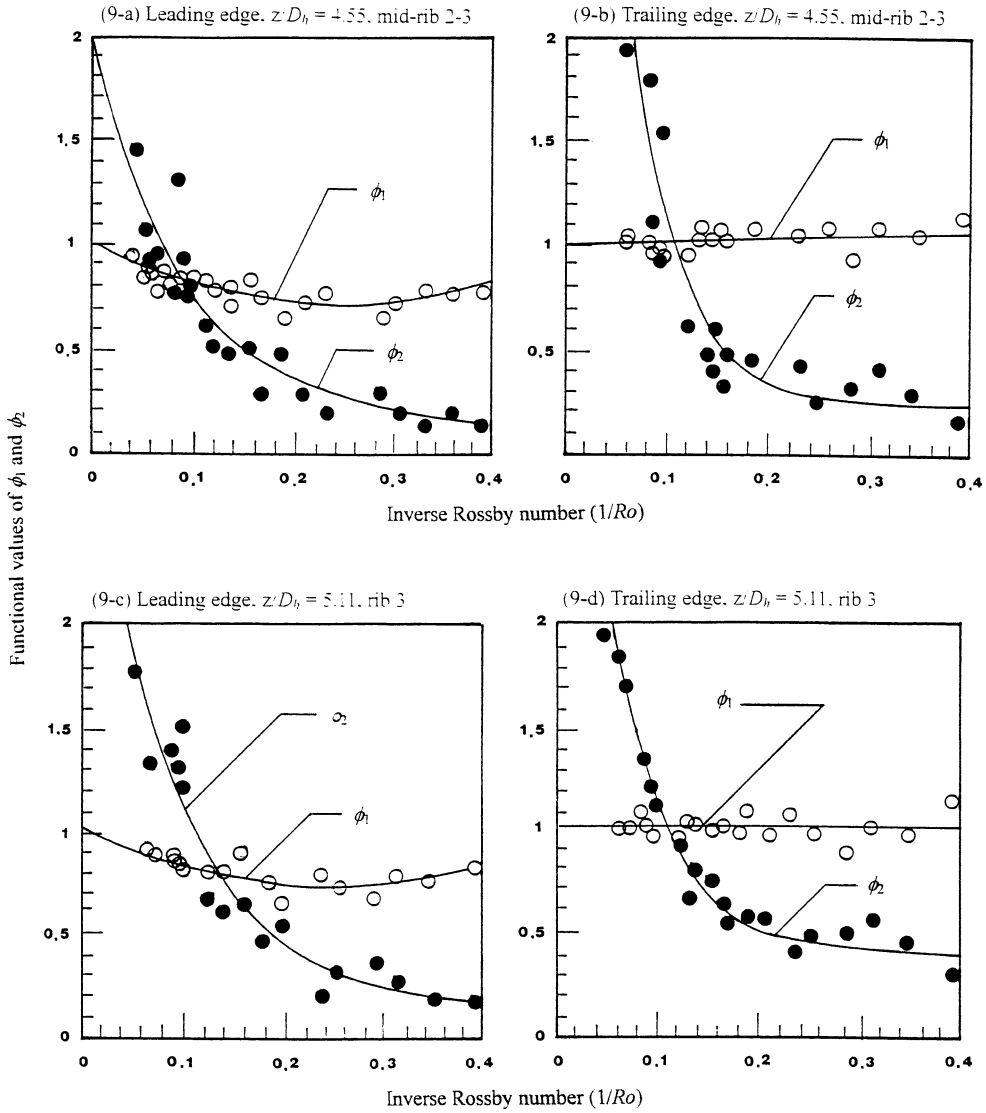


Fig. 9. Variotions of $\phi_1$ and functions with inverse Rossby number at locations of mid-rib 2-3 and rib 3.

likely effect of combined interactions of rib, convective inertial forces, Coriolis-induced secondary flows and centripetal buoyancy on heat transfer over the centerlines of leading and trailing surfaces of a rib-roughened rotating duct.

## 4. Conclusions

The evaluation of heat transfer in a radially rotating square duct fitted with transverse ribs is a formidable task owing to the complex interactions between the normal forced convection, rib-associated flows and the combined Coriolis and centripetal buoyancy effects. With considerations of physical and theoretical consistencies, this paper illustrates a systematic experimental strategy, from the design of experimental apparatus to the detailed analysis of the resulting derived data, that shall be applied to construct the heat transfer correlations and uncouple each dynamic force effects involved. The net result has been an empirical equation embodied in Eq. (18), which may be used to estimate rotational Nusselt numbers along the centerlines of leading and trailing surfaces of a rotating rib-roughened square duct.

The detailed measurements of local heat transfer along the centerlines of leading and trailing surfaces have been acquired and analyzed and, as well as reconfirmation, the Coriolis and centripetal buoyancy forces interactively provide significant heat transfer modification from non-rotational state. In this respect the individual effects of Coriolis and centripetal buoyancy have been independently assessed and the zero buoyancy condition evaluated by extrapolation. With test system been pressurized, the range of the non-dimensional parameters governing this heat transfer regime have been extended into the lower range expected in real engine and also a design-type heat transfer correlation has been generated. In what follows, the important points those have been identified from this experimental investigation are summarized.

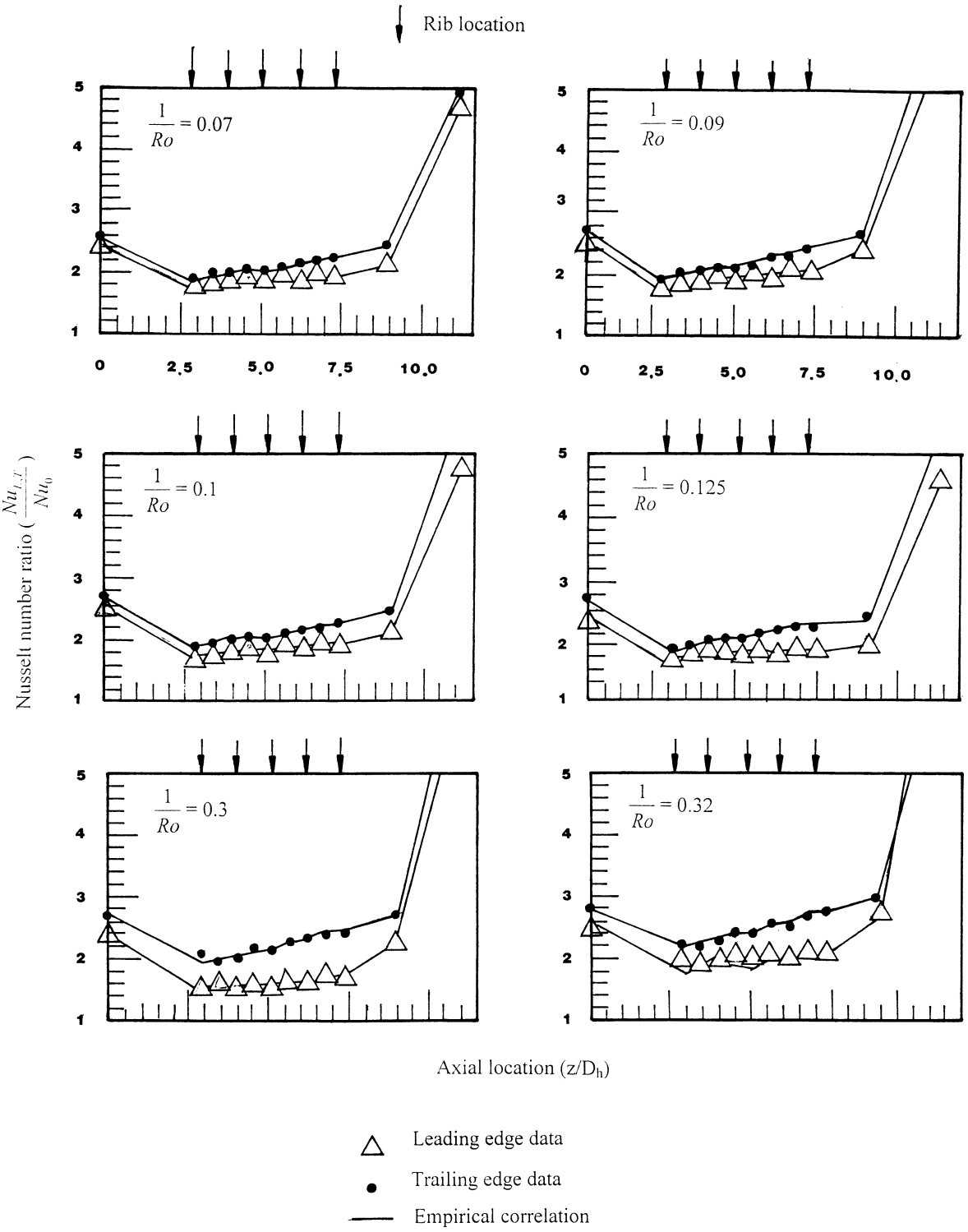


Fig. 10. Comparison of experimental measurements with correlative predictions.

(1) With the ribbed square-sectioned duct the non-rotating local heat transfer variation exhibits a "saw-tooth" pattern particularly defined by the chosen locations of the wall-thermocouples with regions of relatively high heat transfer in the mid-rib locations. The overall heat transfer augmentation due to these transverse ribs is of the order about 2.5 times of the Dittus–Boelter value for smooth-walled duct with similar hydraulic diameter.

(2) Even with the agitated flow field caused by ribs, the significant rotational effects occur in a manner to generate peripheral heat transfer variation with relative high

heat transfer on the trailing edge compared to that on the leading counterpart due to the Coriolis secondary flows. At a specific combination of Reynolds and inverse Rossby numbers, increasing the centripetal buoyancy effect produces increased local heat transfer on the leading and trailing surfaces.

(3) The isolation of forced convection from Coriolis and centripetal buoyancy effects using the Reynolds number scaling idea with the Reynolds number exponent taken from the non-rotating Nusselt number correlation on each rib cell location has been successfully demonstrated. This enables a great simplification of the quest for a correlating equation along the lines of Eq. (18).

(4) By extrapolating the experimental data to the implied zero buoyancy condition, it has been possible, to isolate the effect of Coriolis and centripetal buoyancy on heat transfer over the leading and trailing surfaces for the rib-affected rotating duct flow. Although the flow conditions at the rib and mid-rib locations are different, the zero buoyancy solutions, uncoupled the individual Coriolis effect without buoyancy, seem to be independent with the axial location in the respect of rotational effect in terms of scaled Nusselt number, $Nu/Nu_0$. On the leading surface, the severe heat transfer impediment almost covers the entire data range tested, but, for the trailing surface, the Coriolis effect becomes beneficial which always enhances heat transfer and significant for the inverse Rossby number greater than 0.2.

(5) The proposed empirical correlations for the measured leading and trailing edges are physically consistent and permit the evaluations of individual and interactive effects of Coriolis force and centripetal buoyancy on heat transfer within a rotating rib-roughened square duct.

## Acknowledgements

This research project was made possible by funding and research facilities from the Defense Research Agency and Rolls Royce Plc. UK, and the award of ORS.

## References

[1] P.H. Rothe, J.P. Johnston, Free shear layer behavior in rotating systems, ASME J. Fluids Engrg. 101 (1979) 117–120.

[2] W.D. Morris, in: Heat Transfer and Fluid Flow in Rotating Coolant Channels, Research Studies Press, 1981, pp. 1–228, ISBN 0 471 10121 4.

[3] R.J. Clifford, W.D. Morris, S.P. Harasgama, An experimental study of local and mean heat transfer in a triangular sectioned duct rotating in the orthogonal mode, ASME J. Engrg. Gas Turbines Power 106 (1984) 661–667.

[4] K.M. Iskakov, V.A. Trushin, The effect of rotation on heat transfer in the radial cooling channels of turbine blades, Thermal Engrg. 32 (1985) 52–55.

[5] J. Guidez, Study of convective heat transfer in a rotating coolant channel, ASME J. Turbomachinery 111 (1989 ) 43–50.

[6] W.D. Morris, Ghavami-Nasr, Heat transfer measurements in rectangular channels with orthogonal mode rotation, ASME J. Turbomachinery 113 (1990) 339–345.

[7] H.P. Berg, D.K. Hennecke, M. Elfert, O. Hein, The effect of rotation on local coolant side flow and heat transfer in turbine blade, in: F.S. Billing (Ed.), Tenth International Symposium in Air Breathing Engines, Nottingham, England, UK, September 1–6, 1991.

[8] M.E. Taslim, L.A. Bondi, D.M. Kercher, An experimental investigation of heat transfer in an orthogonally rotating channel roughened with 45 deg criss-cross ribs on two opposite walls, ASME J. Turbomachinery 113 (1991) 346–353.

[9] T.J. Hajek, J.H. Wagner, B.V. Johnson, A.W. Higgins, G.D. Steuber, Effects of rotation on coolant passage heat transfer, Vol. I—Coolant passage with smooth wall, NASA Contract Report, 4396, 1991.

[10] B.V. Johnson, J.H. Wagner, G.D. Steuber, Effects of rotation on coolant passage heat transfer, Vol. II—Coolant passage with trips normal and skewed to the flow, NASA Contract Report, 4396, 1993.

[11] W.D. Morris, R. Salemi, An attempt to experimentally uncouple the effect of Coriolis and buoyancy forces on heat transfer in smooth tubes which rotate in the orthogonal mode, ASME J. Turbomachinery 114 (1992 ) 858–864.

[12] J.C. Han, Y.M. Zhang, Kalkuehler, Kathrin, Uneven wall temperature effect on local heat transfer in a rotating two-pass square channel with smooth walls, ASME J. Heat Transfer 115 (1993) 912–920.

[13] B.V. Johnson, J.H. Wagner, G.D. Steuber, F.C. Yeh, Heat transfer in rotating serpentine passages with trips skewed to the flow, ASME J. Turbomachinery 116 (1994) 113–123.

[14] J.A. Parsons, J.C. Han, Y.M. Zhang, Wall heating effect on local heat transfer in a rotating two-pass square channel with 90° rib turbulators, Internat. J. Heat Mass Transfer 37 (9) (1994) 1411–1420.

[15] S. Dutta, J.C. Han, Local heat transfer in rotating smooth and ribbed two-pass square channels with three channel orientations, ASME J. Heat Transfer 118 (1996) 578–584.

[16] W.D. Morris, S.W. Chang, An experimental study of heat transfer in a simulated turbine blade cooling passage, Internat. J. Heat Mass Transfer 20 (15) (1997) 3703–3716.

[17] W.D. Morris, S.W. Chang, Heat transfer in a radially rotating smooth-walled tube, Aeronautical J. Ser. B 102 (1015) (1998) 277–285.

[18] Y.J. Jang, H.C. Chen, J.C. Han, Flow and heat transfer in a rotating square channel with 45 deg angled ribs by Reynolds stress turbulence model, ASME J. Turbomachinery 123 (2001) 124–131.

[19] B. Metais, E.R.G. Eckert, Forced, mixed and free convection regimes, ASME J. Heat Transfer 86 (1964) 295–296.

[20] W.D. Morris, The design, manufacture and commissioning of a rotating test facility to study the effect of rotation on heat transfer in the cooling passages of turbine rotor blades, Contract Report for the Science and Engineering Research Council, GR/F/261888, UK, 1995.

[21] Editorial Board of ASME Journal of Heat Transfer, Journal of heat transfer policy on reporting uncertainties in experimental measurements and results, ASME J. Heat Transfer 115 (1993) 5–6.

[22] J.C. Han, J.S. Park, C.K. Lei, Heat transfer and pressure drop in blade cooling channels with turbulence promoters, NACA Contract report 3837, 1984.

[23] F.W. Dittus, L.M.K. Boelter, Californian pubs, Engrg. 2 (1936 ) 443.

[24] S.W. Chang, An experimental study of heat transfer in the cooling passage of gas turbine rotor blades, Ph.D. Thesis, University of Wales, Swansea, UK, 1995, pp. 125–126.